NANO LETTERS

pubs.acs.org/NanoLett

Letter

Controlling Umklapp Scattering in a Bilayer Graphene Moiré Superlattice

Mohit Kumar Jat, Shubhankar Mishra, Harsimran Kaur Mann, Robin Bajaj, Kenji Watanabe, Takashi Taniguchi, H. R. Krishnamurthy, Manish Jain, and Aveek Bid*

Cite This: *Nano Lett.* 2024, 24, 2203−2209

Read Online

ACCESS | Metrics & More | Article Recommendations | Supporting Information

ABSTRACT: We present experimental findings on electron−electron scattering in two-dimensional moiré heterostructures with a tunable Fermi wave vector, reciprocal lattice vector, and band gap. We achieve this in high-mobility aligned heterostructures of bilayer graphene (BLG) and hBN. Around the half-full point, the primary contribution to the resistance of these devices arises from Umklapp electron−electron (Uee) scattering, making the resistance of graphene/hBN moiré devices significantly larger than that of non-aligned devices (where Uee is forbidden). We find that the strength of Uee scattering follows a universal scaling with Fermi energy and is nonmonotonically dependent on the superlattice period. The Uee scattering can be tuned with the electric field and is affected by layer polarization of BLG. It has a strong particle−hole asymmetry; the resistance when the chemical potential is in the conduction band is significantly lower than when it is in the valence band, making the electron-doped regime more practical for potential applications.

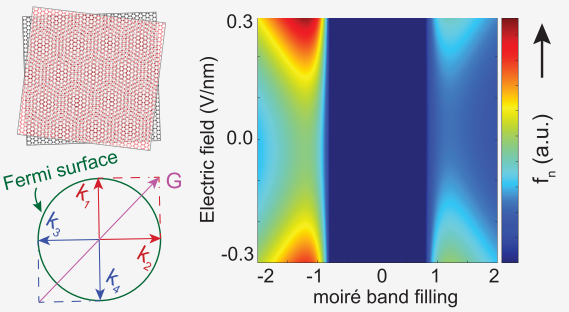

KEYWORDS: *Umklapp scattering, bilayer graphene, moiré superlattice, layer polarization, Brown−Zak oscillations*

In a Galilean-invariant electron liquid, normal electron−electron scattering does not cause a loss of the momentum imparted to the electrons by the driving electric field; consequently, it cannot lead to electrical resistance. A realistic Fermi liquid is, however, not Galilean-invariant; a finite coupling to an underlying lattice provides a mechanism for the momentum relaxation of the quasiparticles via the Umklapp process.[1] Umklapp electron−electron (Uee) scattering is the fundamental mechanism that allows the transfer of momentum from electrons to the lattice and imparts electrical resistance to the metal.[2−8] In this process, the crystal lattice gives a momentum kick to a pair of interacting electrons, backscattering them on the other side of the Fermi surface. Their quasimomentum is conserved, modulo a reciprocal lattice vector **G**

$$\mathbf{k}_1 + \mathbf{k}_2 = \mathbf{k}_3 + \mathbf{k}_4 + \mathbf{G} \quad (1)$$

where $\hbar\mathbf{k}_1$ and $\hbar\mathbf{k}_2$ and $\hbar\mathbf{k}_3$ and $\hbar\mathbf{k}_4$ are the initial and final quasimomenta of the two electrons near the Fermi level, respectively, and **G** is a non-zero reciprocal lattice vector of the crystal. This stringent conservation constraint, coupled with the lack of tunability of the Fermi wave vector, makes experimental identification of Uee processes in normal metals challenging.[7−9] Notable exceptions are heavy-Fermionic systems whose large effective quasiparticle mass leads to an appreciable Uee-mediated resistance at very low temperatures (≈100 mK).[10]

In the limit of nearly free electrons, one can view the Uee scattering as a two-stage process. In the first step, an electron−hole pair is excited into a virtual state by an electron, followed by the scattering of one of these particles by the periodic lattice potential. The temperature dependence of the Uee scattering process at a finite temperature is thus set by the size of the scattering phase space ($\propto k_B T/E_F$) for each electron; only the quasiparticles residing within a width of order $k_B T$ around Fermi energy E_F can undergo binary collisions. Consequently, the contribution of Uee to the sheet resistance in two dimensions goes as $R_{\square_{Uee}} = f_n T^2$.[11] $f_n \propto E_F^{-2}$ is a material-dependent parameter.[12−14]

Note, however, that Uee need not be the only source of T^2 resistivity in a material.[13,15−18] A claim that the dominant source of scattering is the Uee process should be backed up by a (1) quantification of prefactor f_n, (2) a demonstration of the scaling of $f_n \propto E_F^{-2}$, and (3) ruling out other competing mechanisms (e.g., electron−phonon scattering[18]) that can give T-dependent charge scattering.

Received: November 3, 2023
Revised: February 7, 2024
Accepted: February 8, 2024
Published: February 12, 2024

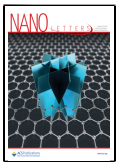

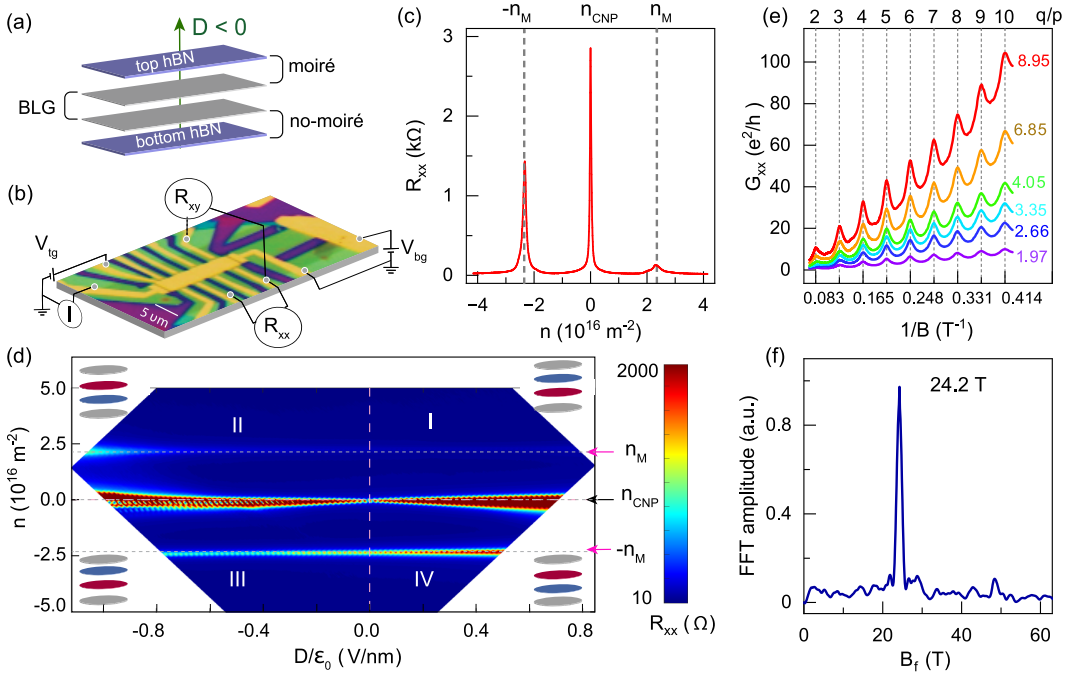

Figure 1. Characteristics of moiré device M1. (a) Schematic of the device layers, indicating moiré (no-moiré) superlattice formation between top hBN (bottom hBN) and BLG. (b) Optical image of the device labeled with the measurement configuration (scale bar of 5 μm). (c) Plot of longitudinal resistance R_{xx} (B = 0) at 2 K as a function of n. Dotted gray lines mark the moiré satellite peaks with a carrier density n_M of $\pm 2.30 \times 10^{16}$ m^{-2}. (d) Two-dimensional map of R_{xx} as a function of n and D. Labels I–IV mark the four quadrants in the n–D plane. The four insets show schematically the charge distribution in the two layers of BLG in these four regimes at high D values. The red (blue) ovals indicate the layers of BLG with the higher (lower) degree of occupation of the electronic states. The upper bound on R_{xx} is set to be 2 kΩ to improve the visibility of the satellite peak (for the complete data, see section S2 of the Supporting Information). (e) Plot of Brown–Zak oscillations G_{xx} vs $1/B$ for different carrier densities (units of 10^{16} m^{-2}) measured at 100 K. (f) Fourier spectrum of the Brown–Zak oscillations measured at an n of 4.05×10^{16} m^{-2} showing a single prominent peak at B_f = 24.2 T.

Graphene-based moiré superlattices[4,6,19−25] provide a system with precise tunability of reciprocal lattice vectors **G** (via the twist angle between the constituent layers) and Fermi wave vectors $\mathbf{k_F}$ (by controlling carrier density n through electrostatic gating). It thus provides a vast phase space in which eq 1 may be satisfied, and the scaling of f_n versus E_F can be verified. Recent calculations (that treat both electron–electron Coulomb interaction and the moiré superlattice potential perturbatively) predict that in aligned heterostructures of Bernal bilayer graphene (BLG) and hBN, Uee scattering processes should be the primary source of resistance.[5]

In this Letter, we experimentally verify that in high-mobility moiré superlattices of BLG and hBN, Uee is the dominant source of resistance near half-filling. Our studies show that the strength of Uee depends nonmonotonically on the superlattice period. This is on par with recent theoretical predictions[5] and in sharp contrast to observations in single-layer graphene-based superlattices.[4] We illustrate the tunability of the strength of the Uee process (quantified by f_n) with displacement field D and carrier density n. Additionally, we demonstrate a strong particle–hole asymmetry in the strength of the Uee process, whose origin can be traced to the moiré potential having a much stronger effect on the valence band than on the conduction band.[4,5] Furthermore, we demonstrate the high tunability of the Umklapp resistivity with an external vertical electric field, emphasizing the potential for precise control over the electronic properties of bilayer graphene superlattices. Finally, we show that these processes are completely absent in non-aligned devices.

High-quality hBN/BLG/hBN heterostructures were fabricated using the dry transfer technique (section S1 of the Supporting Information).[26−28] The top hBN was aligned at nearly 0° with BLG, and the bottom hBN was intentionally misaligned to a large angle to ensure that a moiré pattern forms only between top hBN and BLG (Figure 1a). The device is in a hall bar geometry (Figure 1b) with dual gates to tune carrier density n and vertical displacement field D independently via the equations $n = (C_{tg}V_{tg} + C_{bg}V_{bg})/e + n_r$ and $D = (C_{tg}V_{tg} - C_{bg}V_{bg})/2 + D_r$, respectively. Here C_{bg} (C_{tg}) is the back-gate (top-gate) capacitance, and V_{bg} (V_{tg}) is the back-gate (top-gate) voltage. n_r and D_r are the residual number density and displacement field in graphene, respectively, due to impurities. The direction of the negative displacement field (D) is marked schematically in Figure 1a. In the text, we provide the data for device M1 (with a twist angle of ≈0° and a superlattice wavelength of 14 nm), unless otherwise mentioned. The data for three more hBN/BLG/hBN superlattice devices, labeled M2–M4 with twist angles of ≈0.26°, 0.47°, and 1.70°, respectively, and superlattice wavelengths of ≈13.64, 12.73, and 7.20 nm, respectively, are presented in the Supporting Information. We also present data for a non-aligned hBN/BLG/hBN device (labeled N1) to compare the T dependence of resistance between Uee-allowed (aligned devices) and Uee-forbidden (non-aligned devices) systems.

Measured longitudinal resistance R_{xx} on device M1 at 2 K shows a peak at the charge neutrality point (CNP), n_{CNP} = 0, and moiré satellite peaks at an n_M of $\pm 2.30 \times 10^{16}$ m^{-2} (Figure 1c). The mobility at CNP is extracted to be 350 000 m^2 V^{-1} s^{-1}. Quantum Hall measurements at a perpendicular magnetic

https://doi.org/10.1021/acs.nanolett.3c04223
Nano Lett. 2024, 24, 2203−2209

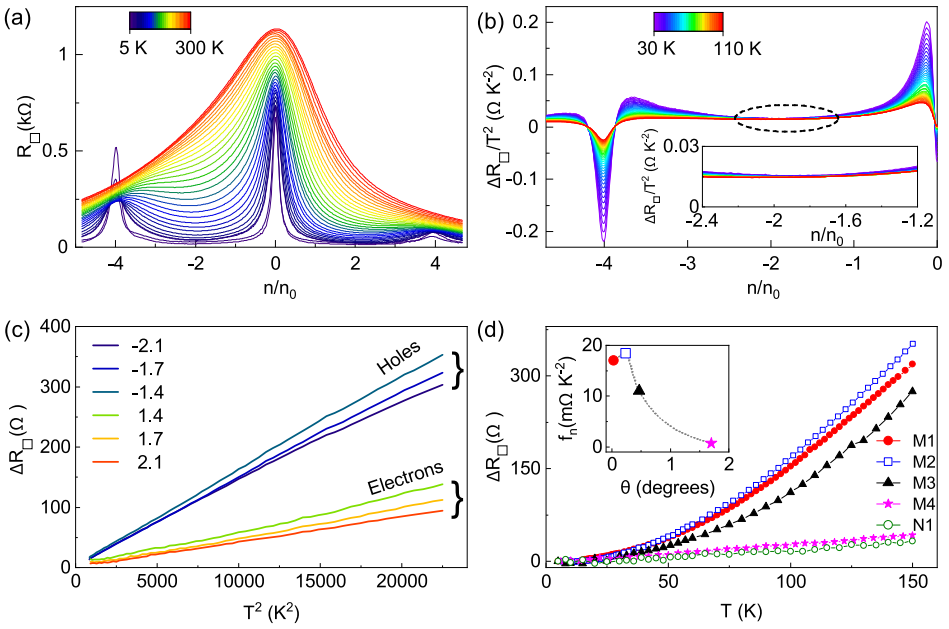

Figure 2. Umklapp scattering at $D/\varepsilon_0 = 0$ V/nm. (a) Plot of sheet resistance $R_\square$ as a function of filling fraction n/n_0 over a range of temperatures from 5 K (blue) to 300 K (red). (b) Plot of $\Delta R_\square/T^2 = [R_\square(T) - R_\square(5K)]/T^2$ vs n/n_0 over a range of temperature from 30 K (blue) to 110 K (red). The dotted ellipse marks the region where Umklapp is the dominant scattering mechanism. The negative value of $\Delta R_\square/T^2$ around $n/n_0 = -4$ is a consequence of the fact that at these number densities, the value of $R_\square$ decreases with an increase in T. The inset shows a close-up view of the region around $n/n_0 = -2$. (c) Plot of $\Delta R_\square$ as a function of T^2 for six different values of n/n_0. (d) Comparison of plots of $\Delta R_\square$ vs temperature at $n/n_0 = -2$ for four aligned devices (M1−M4) with twist angles (0°, 0.26°, 0.47°, and 1.70°) and non-aligned device N1 at $n = -1 \times 10^{16}$ m^{-2}. The inset shows the dependence of f_n on the moiré twist angle θ (measured in degrees). The dashed line is a guide for the eyes.

field (B) of 5 T establish that both spin and valley degeneracies are lifted, indicating the high quality of the device (section S5 of the Supporting Information); these measurements are used to calibrate the values of C_{bg} and C_{tg}. The angle homogeneity of the device is ascertained by comparing the R_{xx} data measured in different configurations (section S2 of the Supporting Information).

Our results for R_{xx} as a function of carrier density n and electric field D/ε_0, shown in Figure 1d, determine that the values of the moiré gap at carrier density n_M are independent of the applied electric field. The plot can be divided into four quadrants labeled I−IV. In quadrants I ($n > 0$; $D/\varepsilon_0 > 0$) and III ($n < 0$; $D/\varepsilon_0 < 0$), at a finite D, the occupied electronic states near the Fermi energy are predominantly localized (marked with a red color oval) in the bottom layer of BLG (away from the moiré interface) and are weakly localized (marked with a blue color oval) in the top layer of BLG (close to the moiré interface). This leads to the suppression of moiré effects and a low resistance value of the satellite peak in these quadrants. The opposite effect is seen in quadrants II ($n > 0$; $D/\varepsilon_0 < 0$) and IV ($n < 0$; $D/\varepsilon_0 > 0$); the occupied electronic states are predominantly localized in the top layer of BLG (close to the moiré interface), leading to the enhancement of moiré effects and higher resistance of the satellite peaks in these quadrants. We explore the consequences of this displacement field-induced layer polarization on Uee scattering below.

The moiré periodicity of the system is estimated from Brown−Zak oscillation measurements at 100 K (Figure 1e). Thermal broadening smears out Landau oscillations at this increased temperature, and only Bloch oscillations survive.[19,29−31] A Fourier spectrum of the oscillations yields the inverse periodicity or the "frequency" of the oscillations (B_f) to be 24.2 T (Figure 1f). The observation of only a single frequency rules out the double alignment of the BLG with hBN.[19,32] Using the relation $S = h/eB_f$ (S being the real-space area of the moiré superlattice cell, h Planck's constant, and e the electronic charge), the moiré wavelength (λ) is calculated to be 14 nm and the carrier density corresponding to filling the bands just up to the moiré gaps ($4/S$) is 2.30×10^{16} m^{-2}; the factor of 4 arises from the 2-fold spin and valley degeneracy of graphene. This value of carrier density matches n_M exactly, validating the number density corresponding to the moiré gap obtained from zero-magnetic field R_{xx} measurements. The twist angle between BLG and hBN corresponding to this moiré wavelength is approximately 0°, indicating the nearly perfect alignment between the top hBN and the BLG.

Figure 2a shows the plots of the zero-magnetic field longitudinal sheet resistance $R_\square = R_{xx}w/l$ (w and l are the width and length of the channel, respectively, where $w/l = 1.5$) versus moiré band filling fraction n/n_0 over a temperature range of 5−300 K at zero displacement field. Here, $n_0 = 1/A = n_M/4$ is the carrier density when the moiré band is one-quarter full. With an increase in temperature, one notices a sharp increase in $R_\square$ around $n/n_0 = -2$ (Figure 2d); this feature is completely absent in non-aligned BLG devices (section S3 of the Supporting Information). As we establish below, this rapid increase in $R_\square$ with T arises from Umklapp scattering in the device.

At $T = 0$, Uee is suppressed, and the resistivity is dominated by disorder scattering.[12] To mitigate the effect of static disorder scattering, we henceforth focus on $\Delta R_\square(T) = R_\square(T) - R_\square(5\text{ K})$. The magnitude of $R_\square(5\text{ K})$ at $n/n_0 = -2$ is ≈14 Ω. Figure 2b shows a plot of $\Delta R_\square/T^2$ versus n/n_0 over a temperature range from 30 to 110 K; the data at all temperatures collapse onto a single curve in the filling fraction

https://doi.org/10.1021/acs.nanolett.3c04223
Nano Lett. 2024, 24, 2203−2209

range $-2 \leq n/n_0 \leq -1$ (marked by the dotted ellipse) showing that $\Delta R_\square \propto T^2$ over this range. This can be better appreciated from the inset, which shows the data over a narrow range around $n/n_0 = -2$. Figure 2c plots $\Delta R_\square$ versus T^2 to better show the electron−hole asymmetry over a range of n/n_0 values. The linearity of the plots of sheet resistance versus T^2 in this carrier density regime persists until about ≃110 K, establishing Uee scattering as the source of resistance (Figure 2c). This temperature is on the order of the Bloch−Grüneisen temperature in graphene. Above this T, electron−phonon scattering starts to become the dominant source of resistance, and the quadratic relation between $\Delta R_\square$ and T breaks down.[33−35] Figure 2d shows a comparison of $\Delta R_\square$ for the five devices; the strong quadratic T dependence seen in aligned devices is completely absent in the non-aligned device where Uee is forbidden from phase-space arguments. The inset of Figure 2d shows f_n versus twist angle for the aligned devices, illustrating that the Umklapp strength is nonmonotonic with twist angle.

To understand the number density limits over which Umklapp processes are seen, recall that at very low n/n_0 values, transport in graphene is dominated by electron−hole puddles;[33,36,37] this gives a practical lower bound of n/n_0 at which e−e scattering is detectable.[5] A more accurate lower limit is obtained by the constraint that the Uee process imposes on Fermi wave vector $\mathbf{k}_F$ (eq 1); this sets a lower bound on $|n/n_0|$ equal to $\pi/(2\sqrt{3}) = 0.91$ (see section S4 of the Supporting Information). At the other extreme, at high number densities, one begins to encounter electron−hole scattering processes at the principal mini band edges because of the moiré-induced van Hove singularity (Figure 3b), which masks the Umklapp scattering process.[5]

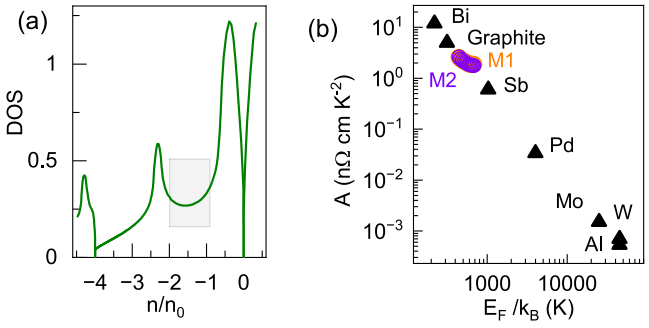

Figure 3. Universal scaling of Umklapp scattering. (a) Plot of the calculated density of states (DOS) vs n/n_0. The shaded area marks the number density range, away from band edges and van Hove singularities, where Uee processes can be unambiguously detected. (b) Plot of $A = f_n t$ vs E_F/k_B. The empty circles are the data from this study on superlattice devices M1 and M2. The filled triangles are the data from ref 12.

Before proceeding further, we eliminate the other probable causes that are known to lead to the T^2 dependence of the resistance. In a system with different carrier types and/or masses (as is the case near the primary and secondary gaps or van Hove singularities), the transfer of momentum between the two carrier reservoirs can lead to a resistivity with T^2 dependence.[38−40] This consideration guides us to avoid filling fractions that lead to Fermi levels close to these regions of the moiré bands and confine our analysis to the filling fraction range $-2 \leq n/n_0 \leq -1$, as shown in Figure 3a. We note that, in low-mobility dilute alloys, the thermal motion of impurity ions can also give rise to a T^2-dependent resistance;[41] this scenario does not apply to our high-mobility heterostructures.

A phenomenological treatment, based on the Rice−Kadowaki−Woods scaling analysis,[13,14] yields

$$f_n \propto \frac{\hbar}{e^2}\left(\frac{k_B}{E_F}\right)^2 \tag{2}$$

In Figure 3b, we plot $A = f_n t$ (t = 0.8 nm is the thickness of BLG) as a function of Fermi energy E_F along with a compilation of data for several different materials.[12] A very good match is obtained, emphasizing the universality of the value of f_n.

Having established Uee as the source of quasiparticle scattering in bilayer graphene/hBN moiré near half-filling ($n/n_0 = -2$), we now shift our focus to the effect of interlayer potential asymmetry (tuned using D) on the Umklapp scattering in quadrants III and IV of Figure 1d. Figure 4a

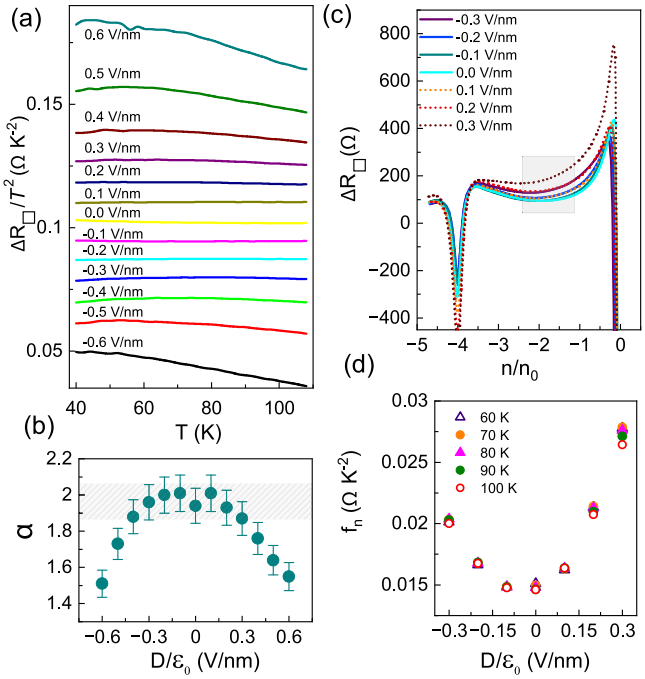

Figure 4. Electric field dependence of Umklapp scattering. (a) Plots of $\Delta R_\square/T^2$ vs T for different values of D/ε_0. The data are for $n/n_0 = -2$. The numbers on the plots are values of D/ε_0. The data have been vertically offset for the sake of clarity. (b) Plot of resistance exponent α [$\alpha = \mathrm{d}\ln(\Delta R_\square)/\mathrm{d}\ln(T)$] vs D/ε_0 at $n/n_0 = -2$. (c) Plot of $\Delta R_\square$ vs filling fraction n/n_0 at 80 K for different values of D/ε_0. (d) Plots of $f_n = \Delta R_\square/T^2$ vs D/ε_0 at a few representative values of T in the Umklapp region at $n/n_0 = -2$.

plots $\Delta R_\square/T^2$ ($n/n_0 = -2$) versus T for several different values of D/ε_0. We find that the temperature exponent of the resistance $\alpha = \mathrm{d}\ln(\Delta R_\square)/\mathrm{d}\ln(T) \approx 2$ for -0.3 V/nm $\leq D/\varepsilon_0 \leq 0.3$ V/nm (Figure 4b). In this D/ε_0 range, we find a substantial increase in scattering strength with D/ε_0, which conforms with theoretical predictions[5] (Figure 4c). Figure 4d plots f_n (D; $n/n_0 = -2$) versus D/ε_0 over the temperature range of 60−100 K. These data points collapse on top of each other with f_n increasing quadratically with D/ε_0.

Note that f_n is slightly asymmetric upon the sign reversal of D/ε_0. To understand this, we recall that the sign of layer polarization in BLG depends on the direction of D. A positive

https://doi.org/10.1021/acs.nanolett.3c04223
Nano Lett. 2024, 24, 2203−2209

D field (as defined in Figure 1a) increases the potential energy of electronic states in the lower layer of BLG compared to those in the top layer of BLG. For negative n values, the occupied electronic states are mainly localized in the top layer of the BLG (that forms the moiré with the hBN).[5] For the negative D field, on the contrary, the occupied electronic states are mainly localized in the bottom layer of the BLG (that does not form the moiré with the hBN). We postulate that the combined effect of this asymmetry of layer polarization on the sign of D and the asymmetry of the moiré potential inherent in this device architecture ultimately manifests as $f_n(D) \neq f_n(-D)$.

With a further increase in the displacement field, α deviates from two, indicating a suppression of Umklapp processes for $|D/\varepsilon_0| > 0.3$ V/nm. We do not have a clear understanding of the origin of this. One plausible reason can be that at large D values, the trigonal warping becomes strong, severely limiting the phase space over which eq 1 may be satisfied.[42] A related effect of the trigonal warping is the formation of overlapping electron−hole bands at certain number densities; the scattering between thermally excited electrons and holes then masks Uee processes.[5,42] A second possible cause of the suppression of Uee at high D values can be the strong modification of the BLG band by the displacement field (this includes layer polarization, the opening of a band gap, and enhanced trigonal warping), leading to strong Zitterbewegung, which becomes the relevant scattering mechanism at large $|D|$ values.[43] Further experimental and theoretical studies are required to verify if any of these is indeed the cause for suppression of Umklapp scattering with an increase in D.

In conclusion, our experiments unequivocally establish Umklapp scattering to be the leading source of resistance in hBN/BLG superlattices in certain filling fraction ranges. Our findings on the hBN/BLG superlattice differ from recent studies of the hBN/SLG superlattice[4] in several significant aspects. In the SLG hBN moiré, R_{Uee} increases monotonically with superlattice period and charge carrier density.[4] In contrast, R_{Uee} in the BLG moiré superlattice is predicted to depend nonmonotonically on the superlattice period.[5] In this Letter, we experimentally verified this prediction. Additionally, bilayer-based systems provide a strong electric field tunability of the band gap and layer polarization and thus have an enormous scope for room-temperature applications.[44−49] We have shown that the strength of Uee increases rapidly with the strength of the displacement field; this fact must be included when designing any D field-controlled superlattice device architectures. Additionally, we find the strength of Uee scattering to be stronger in the BLG/hBN superlattice than in the SLG/hBN superlattice (section S6 of the Supporting Information).

With the presently available technology, the best quality BLG field effect devices are formed when encapsulated between a crystalline insulator, like hBN.[50−52] As the growth of graphene in hBN leads to aligned layers,[53−55] it is imperative to understand the significant sources of Joule heating in such systems for optimal room-temperature operations. This study achieves this and should motivate further studies in related systems like twisted bilayer graphene and twisted bilayers of transition metal dichalcogenides.

While this Letter was under review, we became aware of a preprint[56] that demonstrates that at $n/n_0 = -2$, transport in the BLG/hBN moiré is dominated by Umklapp scattering.

■ ASSOCIATED CONTENT

Supporting Information

The Supporting Information is available free of charge at https://pubs.acs.org/doi/10.1021/acs.nanolett.3c04223.

Device fabrication (section S1), twist angle estimation (section S2), comparison of sheet resistance between moiré and non-moiré devices (section S3), calculation of the threshold density (section S4), quantum Hall effect of the device (section S5), comparision of Umklapp strength in the hBN moiré of BLG and SLG (section S6), and supplementary references (PDF)

■ AUTHOR INFORMATION

Corresponding Author

Aveek Bid − *Department of Physics, Indian Institute of Science, Bangalore 560012, India;* orcid.org/0000-0002-2378-7980; Email: aveek@iisc.ac.in

Authors

Mohit Kumar Jat − *Department of Physics, Indian Institute of Science, Bangalore 560012, India*

Shubhankar Mishra − *Department of Physics, Indian Institute of Science, Bangalore 560012, India*

Harsimran Kaur Mann − *Department of Physics, Indian Institute of Science, Bangalore 560012, India*

Robin Bajaj − *Department of Physics, Indian Institute of Science, Bangalore 560012, India*

Kenji Watanabe − *Research Center for Electronic and Optical Materials, National Institute for Materials Science, Tsukuba 305-0044, Japan;* orcid.org/0000-0003-3701-8119

Takashi Taniguchi − *Research Center for Materials Nanoarchitectonics, National Institute for Materials Science, Tsukuba 305-0044, Japan;* orcid.org/0000-0002-1467-3105

H. R. Krishnamurthy − *Department of Physics, Indian Institute of Science, Bangalore 560012, India*

Manish Jain − *Department of Physics, Indian Institute of Science, Bangalore 560012, India;* orcid.org/0000-0001-9329-6434

Complete contact information is available at: https://pubs.acs.org/10.1021/acs.nanolett.3c04223

Author Contributions

M.K.J., S.M., H.K.M., and A.B. conceived the idea of the study, conducted the measurements, and analyzed the results. T.T. and K.W. provided the hBN crystals. R.B., M.J., and H.R.K. developed the theoretical model. All of the authors contributed to the preparation of the manuscript.

Notes

The authors declare no competing financial interest.

■ ACKNOWLEDGMENTS

A.B. acknowledges funding from U.S. Army DEVCOM Indo-Pacific (Project FA5209 22P0166) and the Department of Science and Technology, Government of India (DST/SJF/PSA-01/2016-17). M.J. and H.R.K. acknowledge the National Supercomputing Mission of the Department of Science and Technology, India, and the Science and Engineering Research Board of the Department of Science and Technology, India, for financial support under Grants DST/NSM/R&D_HPC Applications/2021/23 and SB/DF/005/2017, respectively. M.K.J. and R.B. acknowledge funding from the Prime

Minister's research fellowship (PMRF), MHRD. S.M. acknowledges funding from the National post doctoral fellowship (N-PDF), SERB. K.W. and T.T. acknowledge support from the JSPS KAKENHI (Grants 21H05233 and 23H02052) and the World Premier International Research Center Initiative (WPI), MEXT, Japan.

REFERENCES

(1) Ashcroft, N. W.; Mermin, N. D. *Solid State Physics*; Holt-Saunders, 1976.
(2) Kaveh, M.; Wiser, N. Electron-electron scattering in conducting materials. *Adv. Phys.* **1984**, *33*, 257−372.
(3) Maebashi, H.; Fukuyama, H. Electrical Conductivity of Interacting Fermions. II. Effects of Normal Scattering Processes in the Presence of Umklapp Scattering Processes. *J. Phys. Soc. Jpn.* **1998**, *67*, 242−251.
(4) Wallbank, J. R.; Krishna Kumar, R.; Holwill, M.; Wang, Z.; Auton, G. H.; Birkbeck, J.; Mishchenko, A.; Ponomarenko, L. A.; Watanabe, K.; Taniguchi, T.; Novoselov, K. S.; Aleiner, I. L.; Geim, A. K.; Fal'ko, V. I. Excess resistivity in graphene superlattices caused by umklapp electron-electron scattering. *Nat. Phys.* **2019**, *15*, 32−36.
(5) Moulsdale, C.; Fal'ko, V. Umklapp electron-electron scattering in bilayer graphene moiré superlattice. *Phys. Rev. B* **2023**, *107*, 144111.
(6) Ishizuka, H.; Levitov, L. Wide-range T2 resistivity and umklapp scattering in moiré graphene. *New J. Phys.* **2022**, *24*, 052001.
(7) Bass, J.; Pratt, W. P.; Schroeder, P. A. The temperature-dependent electrical resistivities of the alkali metals. *Rev. Mod. Phys.* **1990**, *62*, 645−744.
(8) Gasparov, V.; Huguenin, R. Electron-phonon, electron-electron and electron-surface scattering in metals from ballistic effects. *Adv. Phys.* **1993**, *42*, 393−521.
(9) Messica, A.; Soibel, A.; Meirav, U.; Stern, A.; Shtrikman, H.; Umansky, V.; Mahalu, D. Suppression of Conductance in Surface Superlattices by Temperature and Electric Field. *Phys. Rev. Lett.* **1997**, *78*, 705−708.
(10) Fisk, Z.; Ott, H. R.; Rice, T. M.; Smith, J. L. Heavy-electron metals. *Nature* **1986**, *320*, 124−129.
(11) MacDonald, A. H.; Taylor, R.; Geldart, D. J. W. Umklapp electron-electron scattering and the low-temperature electrical resistivity of the alkali metals. *Phys. Rev. B* **1981**, *23*, 2718−2730.
(12) Behnia, K. On the Origin and the Amplitude of T-Square Resistivity in Fermi Liquids. *Ann. Phys.* **2022**, *534*, 2100588.
(13) Lin, X.; Fauqué, B.; Behnia, K. Scalable T^2 resistivity in a small single-component Fermi surface. *Science* **2015**, *349*, 945−948.
(14) Wang, J.; Wu, J.; Wang, T.; Xu, Z.; Wu, J.; Hu, W.; Ren, Z.; Liu, S.; Behnia, K.; Lin, X. T-square resistivity without Umklapp scattering in dilute metallic Bi2O2Se. *Nat. Commun.* **2020**, *11*, 3846.
(15) van der Marel, D.; van Mechelen, J. L. M.; Mazin, I. I. Common Fermi-liquid origin of T^2 resistivity and superconductivity in *n*-type $SrTiO_3$. *Phys. Rev. B* **2011**, *84*, 205111.
(16) Ando, Y.; Komiya, S.; Segawa, K.; Ono, S.; Kurita, Y. Electronic Phase Diagram of High-T_c Cuprate Superconductors from a Mapping of the In-Plane Resistivity Curvature. *Phys. Rev. Lett.* **2004**, *93*, 267001.
(17) Maslov, D. L.; Chubukov, A. V. Optical response of correlated electron systems. *Rep. Prog. Phys.* **2017**, *80*, 026503.
(18) Trofimenkoff, P. N.; Ekin, J. W. Electron-Phonon Umklapp Scattering Processes in the Low-Temperature Ultrasonic Attenuation and Electrical Resistivity of Potassium. *Phys. Rev. B* **1971**, *4*, 2392−2397.
(19) Jat, M. K.; Tiwari, P.; Bajaj, R.; Shitut, I.; Mandal, S.; Watanabe, K.; Taniguchi, T.; Krishnamurthy, H. R.; Jain, M.; Bid, A. Higher-order Bragg gaps in the electronic band structure of bilayer graphene renormalized by recursive supermoiré potential. *arXiv* **2023**, DOI: 10.48550/arXiv.2304.01720.
(20) Ponomarenko, L. A.; et al. Cloning of Dirac fermions in graphene superlattices. *Nature* **2013**, *497*, 594−597.
(21) Kuiri, M.; Srivastav, S. K.; Ray, S.; Watanabe, K.; Taniguchi, T.; Das, T.; Das, A. Enhanced electron-phonon coupling in doubly aligned hexagonal boron nitride bilayer graphene heterostructure. *Phys. Rev. B* **2021**, *103*, 115419.
(22) Wang, Z.; et al. Composite super-moire lattices in double-aligned graphene heterostructures. *Sci. Adv.* **2019**, *5*, eaay8897.
(23) Finney, N. R.; Yankowitz, M.; Muraleetharan, L.; Watanabe, K.; Taniguchi, T.; Dean, C. R.; Hone, J. Tunable crystal symmetry in graphene-boron nitride heterostructures with coexisting moiré superlattices. *Nat. Nanotechnol.* **2019**, *14*, 1029−1034.
(24) Yang, Y.; Li, J.; Yin, J.; Xu, S.; Mullan, C.; Taniguchi, T.; Watanabe, K.; Geim, A. K.; Novoselov, K. S.; Mishchenko, A. In situ manipulation of van der Waals heterostructures for twistronics. *Sci. Adv.* **2020**, *6*, eabd3655.
(25) Yankowitz, M.; Xue, J.; Cormode, D.; Sanchez-Yamagishi, J. D.; Watanabe, K.; Taniguchi, T.; Jarillo-Herrero, P.; Jacquod, P.; LeRoy, B. J. Emergence of superlattice Dirac points in graphene on hexagonal boron nitride. *Nat. Phys.* **2012**, *8*, 382−386.
(26) Tiwari, P.; Sahani, D.; Chakraborty, A.; Das, K.; Watanabe, K.; Taniguchi, T.; Agarwal, A.; Bid, A. Observation of the Time-Reversal Symmetric Hall Effect in Graphene−WSe2 Heterostructures at Room Temperature. *Nano Lett.* **2023**, *23*, 6792−6798.
(27) Amin, K. R.; Nagarajan, R.; Pandit, R.; Bid, A. Multifractal Conductance Fluctuations in High-Mobility Graphene in the Integer Quantum Hall Regime. *Phys. Rev. Lett.* **2022**, *129*, 186802.
(28) Tiwari, P.; Jat, M. K.; Udupa, A.; Narang, D. S.; Watanabe, K.; Taniguchi, T.; Sen, D.; Bid, A. Experimental observation of spin-split energy dispersion in high-mobility single-layer graphene/WSe2 heterostructures. *npj 2D Mater. Appl.* **2022**, *6*, 68.
(29) Hofstadter, D. R. Energy levels and wave functions of Bloch electrons in rational and irrational magnetic fields. *Phys. Rev. B* **1976**, *14*, 2239−2249.
(30) Krishna Kumar, R.; Mishchenko, A.; Chen, X.; Pezzini, S.; Auton, G.; Ponomarenko, L.; Zeitler, U.; Eaves, L.; Fal'ko, V.; Geim, A. High-order fractal states in graphene superlattices. *Proc. Natl. Acad. Sci. U. S. A.* **2018**, *115*, 5135−5139.
(31) Huber, R.; Steffen, M.-N.; Drienovsky, M.; Sandner, A.; Watanabe, K.; Taniguchi, T.; Pfannkuche, D.; Weiss, D.; Eroms, J. Band conductivity oscillations in a gate-tunable graphene superlattice. *Nat. Commun.* **2022**, *13*, 2856.
(32) Wang, Z.; et al. Composite super-moiré; lattices in double-aligned graphene heterostructures. *Sci. Adv.* **2019**, *5*, eaay8897.
(33) Nam, Y.; Ki, D.-K.; Soler-Delgado, D.; Morpurgo, A. F. Electron-hole collision limited transport in charge-neutral bilayer graphene. *Nat. Phys.* **2017**, *13*, 1207−1214.
(34) Laitinen, A.; Kumar, M.; Oksanen, M.; Plaçais, B.; Virtanen, P.; Hakonen, P. Coupling between electrons and optical phonons in suspended bilayer graphene. *Phys. Rev. B* **2015**, *91*, 121414.
(35) Ochoa, H.; Castro, E. V.; Katsnelson, M. I.; Guinea, F. Temperature-dependent resistivity in bilayer graphene due to flexural phonons. *Phys. Rev. B* **2011**, *83*, 235416.
(36) Chen, J.-H.; Jang, C.; Adam, S.; Fuhrer, M. S.; Williams, E. D.; Ishigami, M. Charged-impurity scattering in graphene. *Nat. Phys.* **2008**, *4*, 377−381.
(37) Kashuba, A. B. Conductivity of defectless graphene. *Phys. Rev. B* **2008**, *78*, 085415.
(38) Baber, W. G. The contribution to the electrical resistance of metals from collisions between electrons. *Proc. R. Soc. A* **1937**, *158*, 383−396.
(39) Xu, Y.; et al. Magnetotransport of dirty-limit van Hove singularity quasiparticles. *Commun. Phys.* **2021**, *4*, 1.
(40) Hlubina, R. Effect of impurities on the transport properties in the Van Hove scenario. *Phys. Rev. B* **1996**, *53*, 11344−11347.
(41) Koshino, S. Scattering of Electrons by the Thermal Motion of Impurity Ions. II. *Prog. Theor. Phys.* **1960**, *24*, 1049−1054.
(42) Seiler, A. M.; Geisenhof, F. R.; Winterer, F.; Watanabe, K.; Taniguchi, T.; Xu, T.; Zhang, F.; Weitz, R. T. Quantum cascade of correlated phases in trigonally warped bilayer graphene. *Nature* **2022**, *608*, 298−302.

https://doi.org/10.1021/acs.nanolett.3c04223
Nano Lett. 2024, 24, 2203−2209

(43) Jung, E.; Park, D.; Park, C.-S. Zitterbewegung in bilayer graphene: Effects of trigonal warping and electric field. *Phys. Rev. B* **2013**, *87*, 115438.
(44) Tiwari, P.; Srivastav, S. K.; Bid, A. Electric-Field-Tunable Valley Zeeman Effect in Bilayer Graphene Heterostructures: Realization of the Spin-Orbit Valve Effect. *Phys. Rev. Lett.* **2021**, *126*, 096801.
(45) Zhang, Y.; Tang, T.-T.; Girit, C.; Hao, Z.; Martin, M. C.; Zettl, A.; Crommie, M. F.; Shen, Y. R.; Wang, F. Direct observation of a widely tunable bandgap in bilayer graphene. *Nature* **2009**, *459*, 820−823.
(46) Icking, E.; Banszerus, L.; Wörtche, F.; Volmer, F.; Schmidt, P.; Steiner, C.; Engels, S.; Hesselmann, J.; Goldsche, M.; Watanabe, K.; Taniguchi, T.; Volk, C.; Beschoten, B.; Stampfer, C. Transport Spectroscopy of Ultraclean Tunable Band Gaps in Bilayer Graphene. *Adv. Electron. Mater.* **2022**, *8*, 2200510.
(47) Taychatanapat, T.; Jarillo-Herrero, P. Electronic Transport in Dual-Gated Bilayer Graphene at Large Displacement Fields. *Phys. Rev. Lett.* **2010**, *105*, 166601.
(48) Zhu, Z.; Carr, S.; Ma, Q.; Kaxiras, E. Electric field tunable layer polarization in graphene/boron-nitride twisted quadrilayer superlattices. *Phys. Rev. B* **2022**, *106*, 205134.
(49) He, Z.; Yu, C.; Liu, Q.; Song, X.; Gao, X.; Guo, J.; Zhou, C.; Cai, S.; Feng, Z. High temperature RF performances of epitaxial bilayer graphene field-effect transistors on SiC substrate. *Carbon* **2020**, *164*, 435−441.
(50) Uwanno, T.; Taniguchi, T.; Watanabe, K.; Nagashio, K. Electrically Inert h-BN/Bilayer Graphene Interface in All-Two-Dimensional Heterostructure Field Effect Transistors. *ACS Appl. Mater. Interfaces* **2018**, *10*, 28780−28788.
(51) Hasan, N.; Kansakar, U.; Sherer, E.; DeCoster, M. A.; Radadia, A. D. Ion-Selective Membrane-Coated Graphene-Hexagonal Boron Nitride Heterostructures for Field-Effect Ion Sensing. *ACS Omega* **2021**, *6*, 30281−30291.
(52) Petrone, N.; Chari, T.; Meric, I.; Wang, L.; Shepard, K. L.; Hone, J. Flexible Graphene Field-Effect Transistors Encapsulated in Hexagonal Boron Nitride. *ACS Nano* **2015**, *9*, 8953−8959.
(53) Tang, S.; Wang, H.; Zhang, Y.; Li, A.; Xie, H.; Liu, X.; Liu, L.; Li, T.; Huang, F.; Xie, X.; Jiang, M. Precisely aligned graphene grown on hexagonal boron nitride by catalyst free chemical vapor deposition. *Sci. Rep.* **2013**, *3*, 2666.
(54) Wang, S.; Crowther, J.; Kageshima, H.; Hibino, H.; Taniyasu, Y. Epitaxial Intercalation Growth of Scalable Hexagonal Boron Nitride/Graphene Bilayer Moiré Materials with Highly Convergent Interlayer Angles. *ACS Nano* **2021**, *15*, 14384−14393.
(55) Summerfield, A.; Davies, A.; Cheng, T. S.; Korolkov, V. V.; Cho, Y.; Mellor, C. J.; Foxon, C. T.; Khlobystov, A. N.; Watanabe, K.; Taniguchi, T.; Eaves, L.; Novikov, S. V.; Beton, P. H. Strain-Engineered Graphene Grown on Hexagonal Boron Nitride by Molecular Beam Epitaxy. *Sci. Rep.* **2016**, *6*, 22440.
(56) Shilov, A. L.; Kashchenko, M. A.; Pantaleón, P. A.; Kravtsov, M.; Kudriashov, A.; Zhan, Z.; Taniguchi, T.; Watanabe, K.; Slizovskiy, S.; Novoselov, K. S.; Fal'ko, V. I.; Guinea, F.; Bandurin, D. A. High-mobility compensated semimetals, orbital magnetization, and umklapp scattering in bilayer graphene moire superlattices. *arXiv* **2023**, DOI: 10.48550/arXiv.2311.05124.

https://doi.org/10.1021/acs.nanolett.3c04223
Nano Lett. 2024, 24, 2203−2209